Paeonol inhibits the progression of intracerebral haemorrhage by mediating the HOTAIR/UPF1/ACSL4 axis

Zheng-Long Jin[1,2,*], Wen-Ying Gao[3,*], Shao-Jun Liao[1], Tao Yu[2], Qing Shi[2], Shang-Zhen Yu[2], and Ye-Feng Cai[4]

Abstract

Intracerebral haemorrhage (ICH) is a devastating subtype of stroke with high morbidity and mortality. It has been reported that paeonol (PAN) inhibits the progression of ICH. However, the mechanism by which paeonol mediates the progression of ICH remains unclear. To mimic ICH *in vitro*, neuronal cells were treated with hemin. An *in vivo* model of ICH was established to detect the effect of paeonol on ferroptosis in neurons during ICH. Cell viability was tested by MTT assay. Furthermore, cell injury was detected by GSH, MDA and ROS assays. Ferroptosis was examined by iron assay. RT-qPCR and western blotting were used to detect gene and protein expression, respectively. The correlation among HOTAIR, UPF1 and ACSL4 was explored by FISH, RNA pull-down and RIP assays. Paeonol significantly inhibited the ferroptosis of neurons in ICH mice. In addition, paeonol significantly reversed hemin-induced injury and ferroptosis in neurons, while this phenomenon was notably reversed by HOTAIR overexpression. Moreover, paeonol notably inhibited ferroptosis in hemin-treated neuronal cells via inhibition of ACSL4. Additionally, HOTAIR bound to UPF1, and UPF1 promoted the degradation of ACSL4 by binding to ACSL4. Furthermore, HOTAIR overexpression reversed paeonol-induced inhibition of ferroptosis by mediating the UPF1/ACSL4 axis. Paeonol inhibits the progression of ICH by mediating the HOTAIR/UPF1/ACSL4 axis. Therefore, paeonol might serve as a new agent for the treatment of ICH.

Introduction

Intracerebral haemorrhage (ICH) accounts for approximately 15% of all strokes and represents almost 50% of stroke mortality worldwide (Zhao et al., 2020). People who undergo ICH treatment have a high incidence of recurrent haemorrhagic stroke, which accounts for a significant elevation in incidence compared with those who first suffer from ICH (Chu et al., 2020). Previous studies have confirmed that the high-risk factors related to ICH are lobar haematoma location, race/ethnicity and apolipoprotein (APOE) gene mutations (chiefly cortical superficial siderosis and cerebral microbleeds) (Lorente et al., 2020; Pasi et al., 2020; Sykora et al., 2020). Since ICH seriously threatens the health of elderly people, it is urgent to develop a new method for the treatment of ICH.

Ferroptosis is a type of programmed cell death that is not consistent with necrosis, apoptosis or autophagy (X.

Sun et al., 2020). Moreover, previous studies have found that ferroptosis can increase the levels of ROS and MDA and the accumulation of iron and reduce the level of

[1]Second Clinical Medical College, Guangzhou University of Chinese Medicine, Guangzhou, P.R. China
[2]Department of Neurology, Affiliated Jiangmen Traditional Chinese Medicine Hospital of Ji'nan University, Jiangmen, P.R. China
[3]Department of TCM Pediatrics, Jiangmen Maternal and Child Health Hospital, Jiangmen, P.R. China
[4]Department of Neurology, The Second Affiliated Hospital of Guangzhou University of Chinese Medicine, Guangzhou, P.R. China

*These authors are co-first authors.

Corresponding Author:
Ye-Feng Cai, Department of Neurology, The Second Affiliated Hospital of Guangzhou University of Chinese Medicine, No. 111, Dade Road, Guangzhou 510120, Guangdong, P.R. China.
Email: caiyfengtg@163.com

GSH (Cassetta et al., 2020). According to previous investigations, ferroptosis is one of the types of cell death participating in ICH (Fang et al., 2020; J. Zhang et al., 2020). Li M et al indicated that inhibition of ferroptosis can attenuate the progression of ICH (M. Li et al., 2020). Based on this background, we speculated that activation of ferroptosis can lead to progression of ICH.

Paeonol (PAN, 2′-hydroxy-4′-methoxyacetophenone) is a natural product that is isolated from the genus *Paeonia* (Morsy et al., 2020). In addition, it has been reported to have an inhibitory effect on the progression of multiple diseases (e.g., hypertension, epilepsy and arthritis) (M. Cai et al., 2020; Shi et al., 2020; Yu et al., 2020). Moreover, it has been previously reported that PAN increased the activity of SOD and decreased the level of MDA in ICH mice (Li et al., 2018). It was suggested that ferroptosis may be involved in PAN-mediated inhibition of ICH progression. However, the correlation between PAN and ferroptosis in ICH remains largely unknown. Since ferroptosis plays a key role in the progression of ICH, the effect of PAN on ferroptosis in ICH needs to be explored.

Some studies have reported that noncoding RNAs (ncRNAs) play important roles in multiple diseases (Kurt et al., 2020; Mi et al., 2020; Xiang et al., 2020). Among these ncRNAs, long noncoding RNAs (lncRNAs) are more than 200 nucleotides in length and have limited or no protein-coding capacity (Liu et al., 2020). In recent years, lncRNAs have been shown to participate in ICH progression. For example, Chen JX et al found that lncRNA Mtss1 promoted inflammatory responses after ICH in mice (J. X. Chen et al., 2020). Zhang et al. indicated that lncRNA Snhg3 exacerbated the symptoms of ICH (Zhang et al., 2019). LncRNA HOX transcript antisense RNA (HOTAIR) has been found to promote hypoxia-induced ischaemic infarct (Yang and Lu, 2016). A previous report indicated that PAN inhibited the expression of HOTAIR (Zhou et al., 2019). Thus, PAN might affect the progression of ICH via regulation of HOTAIR. Nevertheless, the underlying mechanism by which HOTAIR affects ICH remains unknown. Moreover, lncRNAs are known to bind to RNA-binding proteins (RBPs), which can disrupt RBP binding of downstream molecular targets (Y. Wang et al., 2020). For instance, it has been reported that UPF1 is mediated by lncRNAs in some diseases (Fefilova et al., 2020; X. Wang et al., 2020). Interestingly, we found that HOTAIR might bind to UPF1. UPF1 is involved in a highly conserved RNA degradation pathway called nonsense-mediated RNA decay (NMD), which can lead to the degradation of mRNAs (Alzahrani et al., 2020; Deka et al., 2020). Based on the above information, we hypothesized that HOTAIR might mediate the progression of ICH by binding to UPF1.

Acyl-CoA Ligase 4 (ACSL4) is a crucial lipid metabolism enzyme that can induce lipid peroxidation and ferroptosis (Cheng et al., 2020; Yuan et al., 2016). A previous report indicated that ACSL4 knockdown inhibited ionizing radiation-induced ferroptosis (Lei et al., 2020). Our research found that UPF1 bound to the HOTAIR and ACSL4 mRNAs. Based on this finding, it can be speculated that HOTAIR may reduce the degradation of ACSL4 by competitively binding to UPF1.

In the current research, we sought to detect the function of PAN in ICH. As expected, we found that PAN inhibited ferroptosis in ICH via the HOTAIR/UPF1/ACSL4 axis. We hope this finding can provide a novel idea for the treatment of ICH.

Materials and Methods

Cell Culture and Treatment

Primary cortical neurons were obtained from embryonic day 15 (E15) CD1 mice. Briefly, cortices were dissected, homogenized, and plated in minimum essential medium containing 10% foetal bovine serum (FBS), 5% horse serum, and 1% penicillin/streptomycin in 96-well plates, 6-well plates, or 10-cm dishes. In addition, a mouse hippocampal neuron cell line (HT22) and 293T cells were obtained from ATCC (Rockville, MD, USA).

All cells were maintained in DMEM (Thermo Fisher Scientific, Waltham, MA, USA) supplemented with 10% FBS (Thermo Fisher Scientific) and antibiotics (100 U/mL penicillin and streptomycin) at 37°C with 5% CO_2.

To mimic ICH *in vitro*, neuronal cells were treated with hemin (Sigma-Aldrich, St. Louis, MO, USA) according to previous references (Hu et al., 2020; Su et al., 2018). PAN and ferrostatin-1 (Fer-1) were obtained from Sigma-Aldrich (St. Louis, MO, USA).

Cell Transfection

pcDNA3.1-HOTAIR, pcDNA3.1-ACSL4, pcDNA3.1-UPF1 and empty vector (pcDNA3.1) were purchased from Guangzhou RiboBio Co., Ltd., and were transfected into neuronal cells ($5\text{x}10^3$) using Lipofectamine® 3000 (Thermo Fisher Scientific). For UPF1 knockdown, 293T cells (5×10^6 cells/well) were transfected with UPF1 shRNA (GenePharma, Shanghai, China) or empty vector (pLVX-IRES-Puro, GenePharma) using Lipofectamine® 3000 reagent (Thermo Fisher Scientific). After transfection, cells were incubated at 37°C for 48 h. Subsequently, the 293T lentiviral supernatant was harvested using centrifugation (956 g, 15 min) and filtered to obtain viral particles. Then, the viral particles were added to neuronal cells (5×10^6 cells/well). After 48 h of transduction, cells were selected with puromycin (Sigma, St. Louis, MA, USA).

MTT Assay

HT22 cells (1×10^6) or cortical neurons were pretreated with PHA (5, 10, 20 or 40 mM) or Fer-1 (1 μM) for 1 h, and then cells were treated with 100 μM hemin for 16 h. Subsequently, cells were treated with 20 μL MTT (Beyotime, Shanghai, China) for 2 h. Then, supernatants of cells were removed, and 100 μL DMSO was added to each well. The OD value at 490 nm was measured by a microplate reader (Thermo Fisher Scientific).

Real-Time Reverse Transcriptase Quantitative PCR (qRT-PCR)

Total RNA was extracted from neuronal cells or brain tissues using TRIzol reagent (Thermo Fisher Scientific). A PrimeScript RT Reagent Kit (TaKaRa, Otsu, Shiga, Japan) was used to reverse transcribe total RNA into cDNA. Then, qRT-PCR was performed by the SYBR® Premix Ex Taq™ II Kit (TaKaRa Bio, Otsu, Shiga, Japan) on a 7900HT System (Applied Biosystems, CA, USA) according to the following conditions: 95°C for 5 min followed by 40 cycles at 95°C for 15 sec, 60°C for 20 sec, and 72°C for 20 sec. The primers used were as follows: HOTAIR: Forward, 5′-GGACCGACGCCT TCCTTATA-3′; Reverse, 5′-TGCGTGTCTTCTGTCC TTCT-3′. UPF1: Forward, 5′-AATGCAAGGAAGTG ACGCTG-3′; Reverse, 5′-AAAGCACCGGTCCTGGA TTA-3′. ACSL4: Forward: 5′-TTGGTCAGGGATAT GGGCTG-3′; Reverse: 5′-GCCACCGACAATCTCAC-3′ and GAPDH: Forward, 5′-AGCCCAAGATGCCC TTCAGT-3′ and Reverse, 5′-CCGTGTTCCTACCCC CAATG-3′. The relative expression levels of target genes were quantified by normalization to GAPDH using the $2^{-\Delta\Delta Ct}$ method.

Western Blot

HT22 cells or cortical neurons were lysed in RIPA Lysis Buffer (KeyGEN, Nanjing, China), and a BCA Assay Kit (Solar Life Science, Beijing, China) was used to detect the protein concentrations. SDS-PAGE (10%) was used to separate equal amounts of protein (30 μg), and the proteins were then transferred onto polyvinylidene difluoride (PVDF) membranes (Thermo Fisher Scientific). Five percent nonfat dried milk in TBST was used to block the PVDF membrane for 1 h. The PVDF membrane was incubated overnight at 4°C with the following primary antibodies: anti-ACSL4 (1:1000, Abcam, Cambridge, MA, USA), anti-UPF1 (1:1000, Abcam), anti-SLC7A11 (1:1000, Abcam), anti-GPX4 (1:1000, Abcam) and anti-β-actin (1:1000, Abcam). Then, the membrane was incubated ith HRP-labelled goat anti-rabbit secondary antibody (1:5000, Abcam) for 1 h. Enhanced chemiluminescence (ECL) reagent (Thermo Fisher Scientific) was used to visualize the protein bands. ImageJ software was used to quantify the intensities of the bands, and β-actin was used for normalization.

RNA-Binding Protein Immunoprecipitation (RIP)

HT22 cells were lysed on ice. The cell supernatant was collected and sonicated after centrifugation. The lysate was incubated with protein Dynabeads (Life Technologies, USA) for 30 min followed by supplementation with the anti-UPF1 antibody or negative control (IgG) and then rotated overnight. Finally, the data were detected by RT-qPCR.

RNA Fluorescence In Situ Hybridization (FISH) and Immunofluorescence

HT22 cells were fixed with 4% paraformaldehyde, incubated and washed for 20 min. Then, the slides were incubated with prehybridization solution (BersinBio, Guangzhou, China) for 30 min. Cy3-labelled HOTAIR probes (GenePharma, Shanghai, China) were denatured for 8 min. Then, the cells were incubated with the anti-UPF1 antibody (ab65334, Abcam) overnight followed by further incubation for 1 h with secondary antibody, and then DNA was labelled with DAPI for 10 min. The data were obtained with a confocal microscope (Olympus, Shinjuku, Japan).

RNA Pull-Down

Biotin RNA Labeling Mix (Roche, Basel, Switzerland) was used to label probe-control or probe-HOTAIR. Secondary structure formation was induced by RNA structure buffer (Thermo, MA, USA) from the biotin-labeled RNAs. Streptavidin beads were washed and then incubated with the biotinylated RNAs overnight. Then, to obtain the streptavidin bead-RNA complexes, the mixture was separated using a magnet. Subsequently, the cell lysates were removed from the complexes and rotated for 1 h.

MDA Detection

The level of MDA in neuronal cells was measured using a Lipid Peroxidation Assay Kit (Abcam) according to the manufacturer's instructions.

GSH Detection

The concentration of GSH in neuronal cells was measured using a Glutathione Assay Kit (Sigma) according to the manufacturer's instructions.

Reactive Oxygen Species (ROS) Detection

Cell suspensions or lipids were collected and supplemented with the ROS probe DCFDA. Then, the cells

or lipids were centrifuged at 30 g, washed with PBS and resuspended. Finally, the relative levels of ROS were measured by FACS.

Iron Assay

The relative iron concentration in neuronal cells was detected using an Iron Assay Kit (Abcam). In brief, cells were collected and washed with cold PBS and then homogenized in 4–10 volumes of Iron Assay Buffer. After removing the insoluble material, 5 μl of iron reducer was added to each well, mixed, and incubated in the dark for 30 min. Subsequently, 100 μl of iron probe was added to each well, mixed, and then incubated for 60 min. The OD was detected at 593 nm using a colorimetric microplate reader. In addition, the total protein concentration in 50 μl samples was quantified using the bicinchoninic acid assay, and the level of Fe^{2+} was calculated.

In Vivo Experiments

C57BL/6 mice (aged 8–10 weeks, Vital River, Beijing, China) were housed in SPF conditions. The animal study was performed according to the National Institutes of Health Guide and approved by the Ethics Committees of Affiliated Jiangmen Traditional Chinese Medicine Hospital of Ji'nan University.

Previous reports indicated that collagenase VII-S induces haemoglobin-mediated oxidative stress in the brain (Cordeiro et al., 2020; Z. Sun et al., 2020). Thus, to establish an *in vivo* model of ICH, the mice (except for those in the sham group) were injected with collagenase VII-S (Sigma-Aldrich) in the left striatum, while the mice in the sham group were injected with saline. After induction with collagenase VII-S, the mice in the PAN-L (10 mg/kg), PAN-M (20 mg/kg) and PAN-H (30 mg/kg) groups were injected intraperitoneally with 5, 10 and 15 mg/kg PAN, respectively. Then, after induction for 1 h, the mice were again injected intraperitoneally with the same amount of PAN. Finally, the mice were sacrificed for brain tissue collection.

Neurological Severity Score and Corner Turn Test

After establishment of the *in vivo* model, a neurological deficit scoring system and corner turn tests were applied to evaluate ICH-induced neurological deficits (Cui et al., 2020; Yoshimoto et al., 2020). During the experimental process, the gait, body symmetry, climbing, front limb symmetry, circling behaviour and compulsory circling of mice were assessed.

Forelimb Placing Test

In the vibrissae-evoked forelimb placing test, mice were held to allow the forelimbs to hang freely. Independent tests were performed on each forelimb by brushing the corresponding whiskers against the edge of the work surface. Uninjured mice quickly place the forelimb ipsilateral to the stimulated whiskers on the work surface. Depending on the degree of injury, the mouse may instead place the forelimb contralateral to the stimulated whiskers on the work surface. The forelimbs of each mouse were tested 10 times, and the percentage of trials in which the suitable forelimb was placed on the edge of the work surface in response to whisker stimulation was determined.

Statistical Analysis

All experiments are expressed as the mean ± standard deviation (SD). Each experiment was repeated three times. Student *t*-test was used for two-group comparisons. One-way analysis of variance (ANOVA) and Tukey's tests were carried out for multiple group comparisons. $P<0.05$ was considered statistically significant.

Results

PAN Inhibited Neuronal Ferroptosis In Vitro and In Vivo

To mimic ICH *in vitro*, HT22 cells were treated with hemin. As shown in Figure 1A, the viability of HT22 cells or primary cortical neurons was notably reduced by hemin and was greatly rescued by PAN (10, 20 and 40 mM) or Fer-1 (Figure 1A). The accumulation of lipid peroxidation products (MDA, ROS) and redox-active iron and the depletion of glutathione (GSH) are the key events in ferroptosis. Hemin-treated HT22 cells or cortical neurons exhibited ferroptotic events that included significantly increased ROS levels, MDA production, GSH consumption and iron accumulation. In contrast, the hemin-induced increases in ROS and MDA levels in HT22 cells or cortical neurons were significantly rescued by PAN (10, 20 and 40 mM) or the ferroptosis inhibitor Fer-1 (Figure 1B and C). Moreover, the level of GSH in hemin-induced HT22 cells or cortical neurons was notably increased by PAN (10, 20 and 40 mM) or Fer-1 (Figure 1D). Consistent with these results, the hemin-induced redox-active iron accumulation in HT22 cells or cortical neurons was inhibited by the three concentrations of PAN and Fer-1 (Figure 1E). Taken together, these data indicate that PAN inhibited ferroptosis in neurons.

PAN Alleviated Neuronal Ferroptosis in ICH Mice

As shown in Figure 2A and B, the neurological severity score and corner turns in ICH mice were decreased by PAN in a dose-dependent manner. In contrast, the
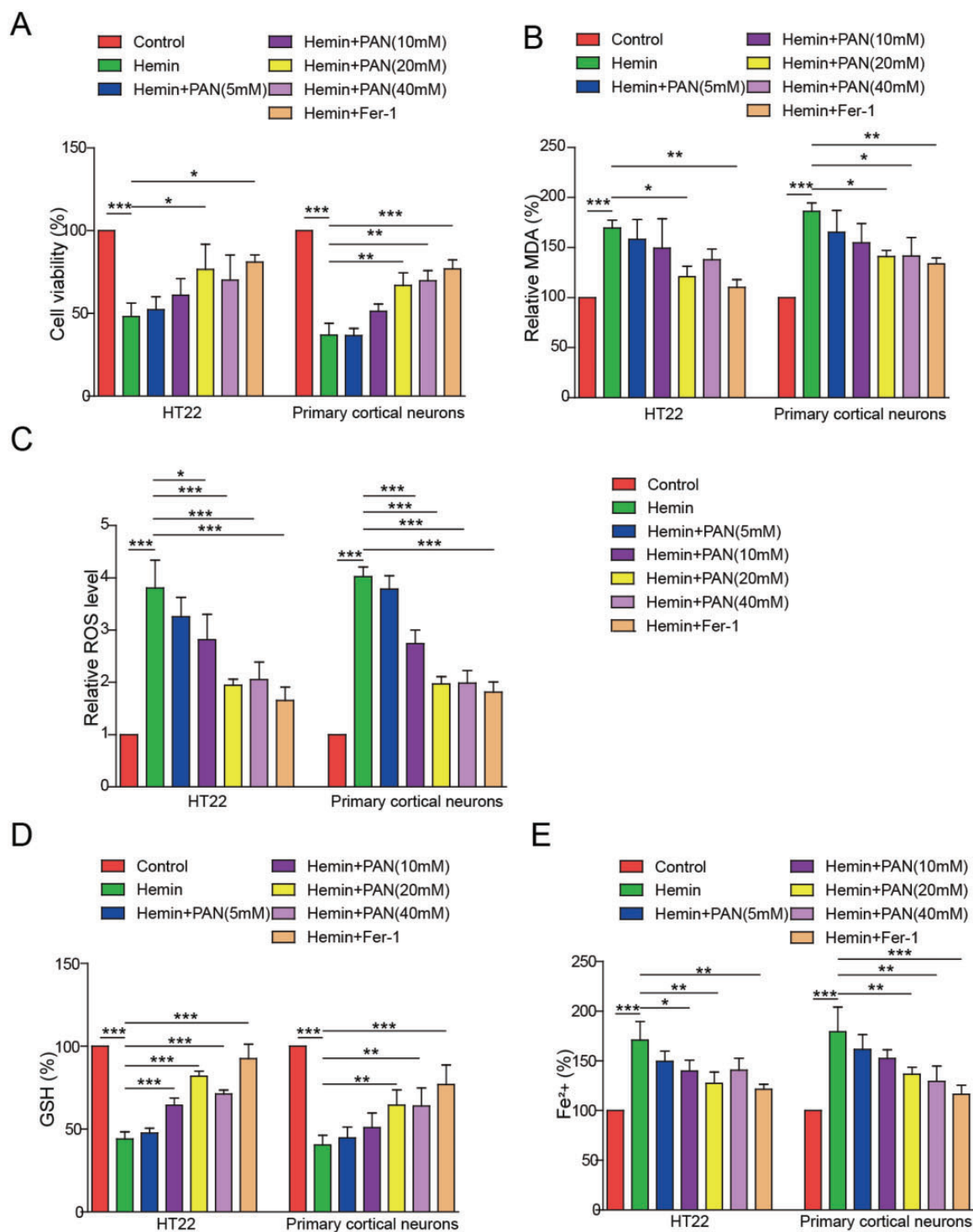
Figure 1. PAN Inhibited Neuronal Ferroptosis *In Vitro*. HT22 cells or primary cortical neurons were pretreated with PAN (5, 10, 20 or 40 mM) or 1 μM Fer-1 for 1 h followed by treatment with 100 μM hemin for 16 h. (A) The viability of neuronal cells was measured by MTT assay. (B) The MDA level in neuronal cells was assessed by a Lipid Peroxidation Assay Kit. (C) The ROS level was detected by flow cytometry. (D) The GSH level in neurons was tested by a Glutathione Assay Kit. (E) The Fe^{2+} content of HT22 cells or cortical neurons was detected by an Iron Assay Kit. $^*P < 0.05$, $^{**}P < 0.01$, $^{***}P < 0.001$. (n = 3 in every group). One-way analysis of variance (ANOVA) and Student's *t*-test were performed to analyse the data.
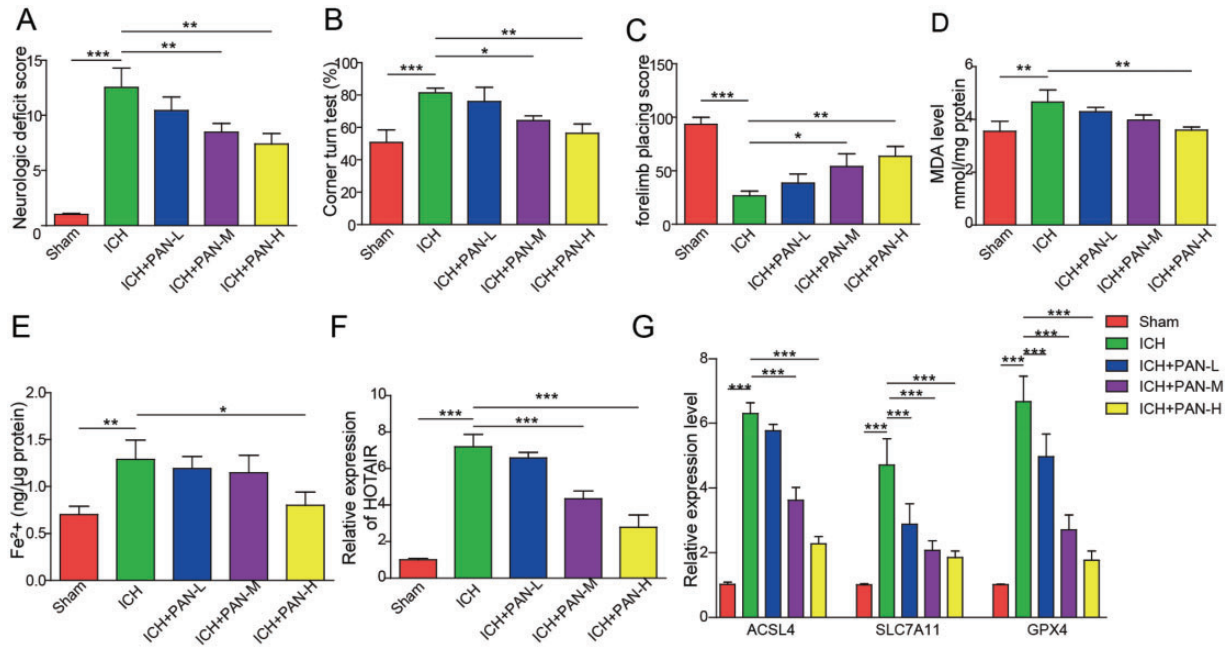
Figure 2. PAN Inhibited Neuronal Ferroptosis *In Vivo*. Mice were induced by collagenase VII-S and treated with three concentrations of PAN. Then, (A) The neurological severity score was evaluated in the mice. (B) Corner turning was tested in the mice. (C) The forelimb placing score of the mice was assessed. (D) The MDA level was tested by a Lipid Peroxidation Assay Kit. (E) The Fe^{2+} content was detected by an Iron Assay Kit. (F) The expression of HOTAIR in mice was assessed by qRT-PCR. (G) The mRNA expression of ACSL4, SLC7A11 and GPX4 in mice was detected by qRT-PCR. $^*P<0.05$, $^{**}P<0.01$, $^{***}P<0.001$. (n = 3 in every group). One-way analysis of variance (ANOVA) and Student's *t*-test were performed to analyse the data.

correct forelimb placement by ICH mice was significantly increased by PAN (Figure 2C). Moreover, 10 or 15 mg/kg PAN significantly decreased the level of MDA and reduced the accumulation of iron in neurons of ICH mice (Figure 2D and E). Additionally, PAN inhibited the expression of HOTAIR and ACSL4, while SLC7A11 and GPX4 were increased by PAN in ICH mice (Figure 2F and G). In summary, PAN reversed neuronal ferroptosis in ICH mice.

HOTAIR Overexpression Reversed the Inhibitory Effect of PAN on HT22 Cell Ferroptosis

To detect the effect of PAN on HOTAIR-expressing neuronal cells, RT-qPCR was performed. As revealed in Figure 3A, the HOTAIR expression in HT22 cells or cortical neurons was significantly increased by hemin, while the effect of hemin was partially reversed by 10, 20 or 40 mM PAN. Since neuronal cells were most sensitive to 20 mM PAN, 20 mM PAN was selected for use in the subsequent experiments. Moreover, PAN-induced inhibition of HOTAIR expression was significantly rescued by HOTAIR overexpression (Figure 3B), and overexpression of HOTAIR significantly reversed the PAN-induced increase in cell viability (Figure 3C). In addition, PAN significantly protected against the hemin-induced ferroptotic injury of neuronal cells,

while the effects of PAN were partially reversed by HOTAIR overexpression (Figure 3D–G). Furthermore, the expression levels of ACSL4 in HT22 cells or cortical neurons were obviously elevated, and SLC7A11 and GPX4 were inhibited by hemin, while PAN greatly reversed the effect of hemin on their expression (Figure 3H). However, the inhibitory effect of PAN on the expression of these three proteins was partially reversed by HOTAIR overexpression (Figure 3H). Overexpression of HOTAIR reversed the ferroptosis inhibition effects of PAN in hemin-treated neurons.

PAN Alleviated ACSL4-Dependent Neuronal Ferroptosis

To detect the expression of ACSL4, qRT-PCR and western blotting were performed. As shown in Figure 4A and B, the expression of ACSL4 in neuronal cells was significantly upregulated by hemin, while this phenomenon was partially reversed by PAN. Moreover, the PAN-induced decrease in ACSL4 expression was significantly rescued by ACSL4 overexpression (Figure 4C). PAN significantly increased the viability of hemin-treated neurons, while this phenomenon was partially reversed by ACSL4 overexpression (Figure 4D). Moreover, as demonstrated in Figure 4E–H, PAN notably alleviated injury and ferroptosis in neuronal cells, and these effects
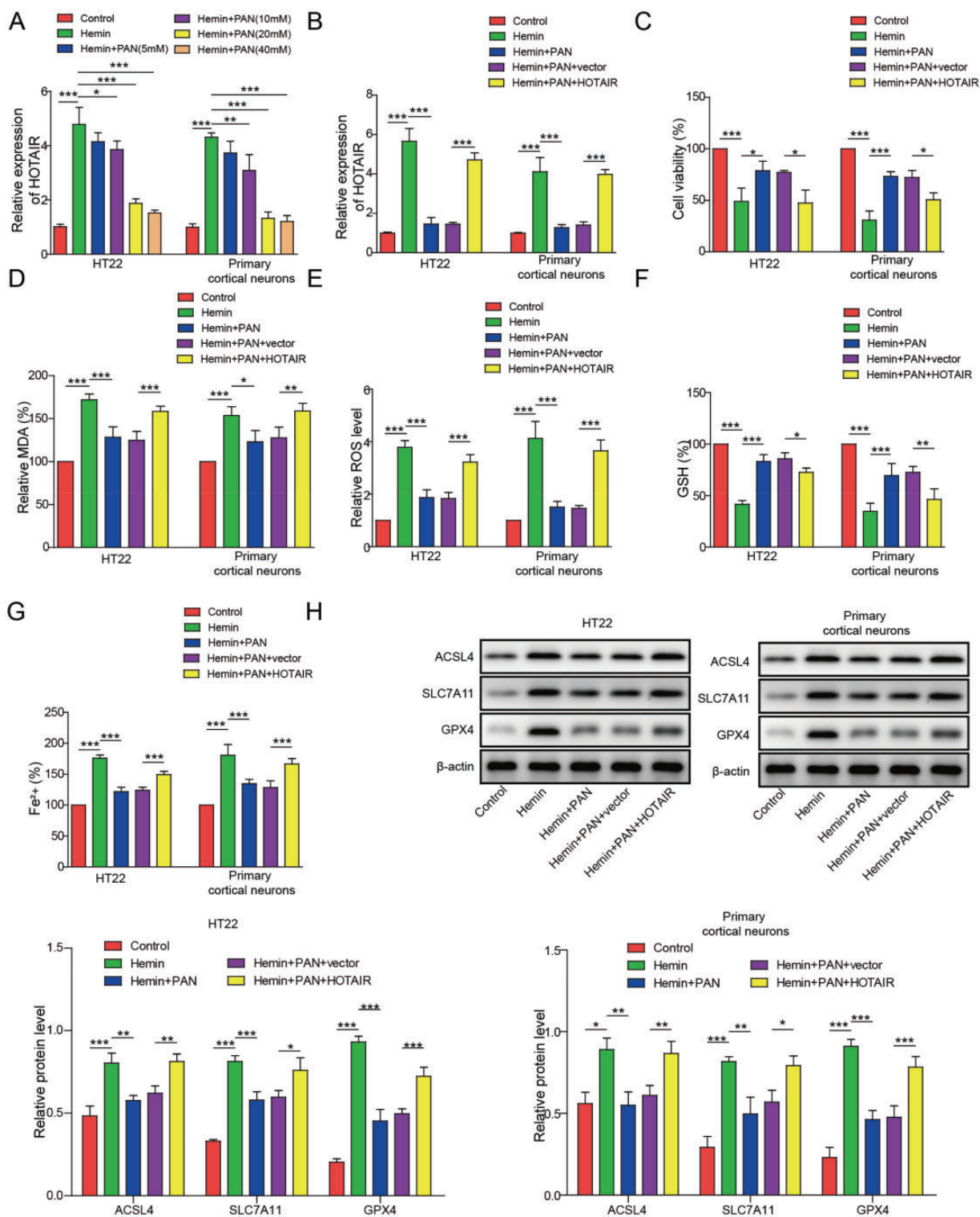
Figure 3. HOTAIR Overexpression Reversed the Inhibitory Effect of PAN on Neuronal Ferroptosis. (A) The expression of HOTAIR in neuronal cells was measured by qRT-PCR. (B) HT22 cells or cortical neurons were transfected with pcDNA3.1-HOTAIR. The expression of HOTAIR in the HT22 cells was measured by qRT-PCR. (C) The viability of neuronal cells was assessed by MTT assay. (D) The level of MDA in neuronal cells was measured by a Lipid Peroxidation Assay Kit. (E) The lipid ROS level was detected by flow cytometry. (F) The GSH level in neuronal cells was detected by a Glutathione Assay Kit. (G) The Fe^{2+} content of neuronal cells was tested by an Iron Assay Kit. (H) ACSL4, SLC7A11 and GPX4 expression in neuronal cells was tested by western blot. β-actin was used for normalization. *$P<0.05$, **$P<0.01$, ***$P<0.001$. (n = 3 in every group). One-way analysis of variance (ANOVA) and Student's t-test were performed to analyse the data.
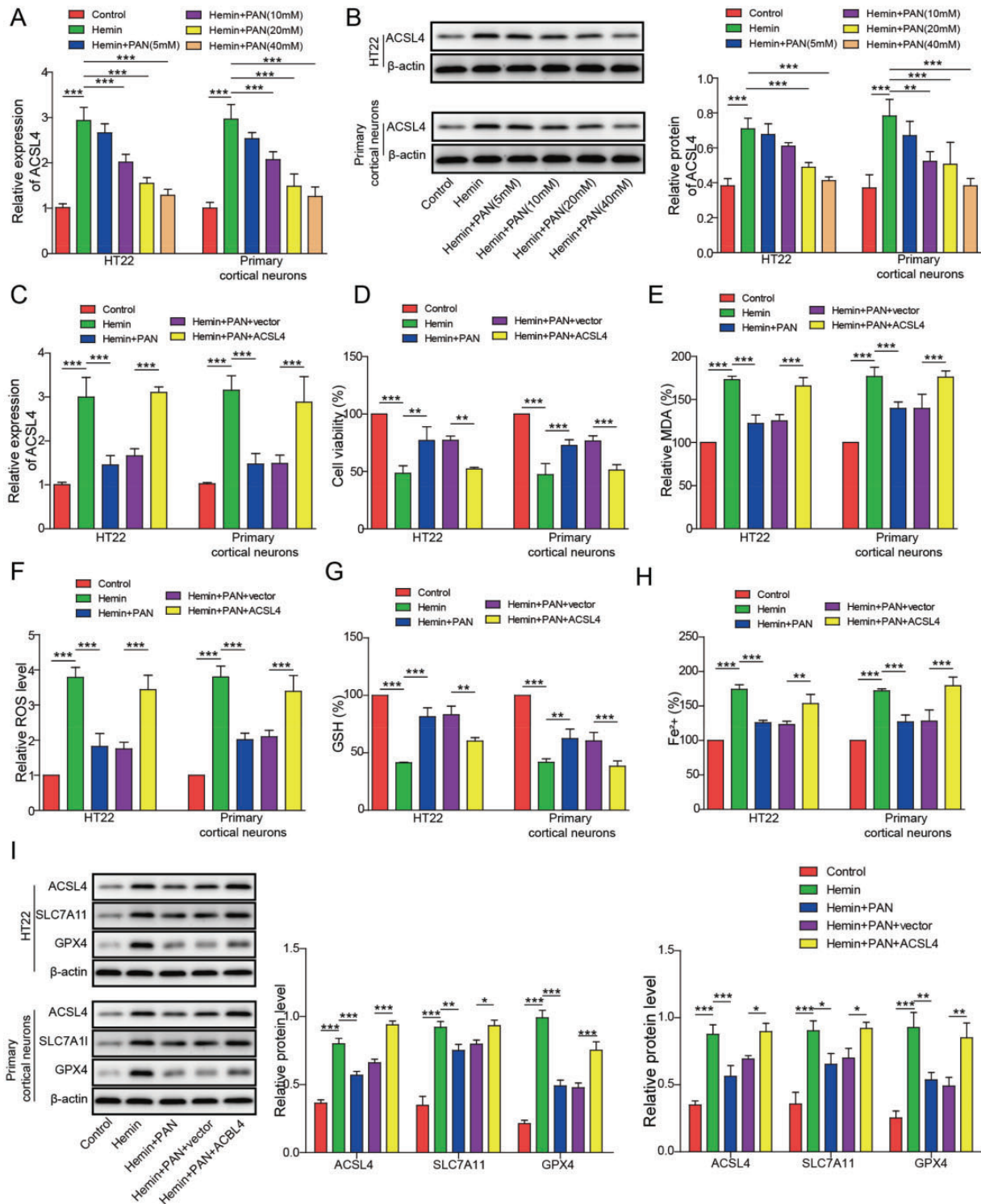
Figure 4. PAN Alleviated ACSL4-Dependent Neuronal Ferroptosis. (A) ACSL4 mRNA levels in neuronal cells were measured by qRT-PCR. (B) ACSL4 expression in neurons was tested by western blot. β-actin was used for normalization. Neuronal cells were transfected with the pcDNA3.1-ACSL4 overexpression vector. Then, (C) ACSL4 mRNA levels in neuronal cells were assessed by qRT-PCR. (D) Neuronal cell viability was tested by MTT assay. (E) The MDA level in neuronal cells was tested by a Lipid Peroxidation Assay Kit. (F) The lipid ROS level was detected by flow cytometry. (G) The GSH level was measured by a Glutathione Assay Kit. (H) The Fe^{2+} content of neurons was assessed by an Iron Assay Kit. (I) ACSL4, SLC7A11 and GPX4 expression was measured by western blot. β-actin was used for normalization. $^{*}P<0.05$, $^{**}P<0.01$, $^{***}P<0.001$. (n = 3 in every group). One-way analysis of variance (ANOVA) and Student's t-test were performed to analyse the data.

were significantly reversed by ACSL4 overexpression (Figure 4E–4H). Furthermore, the expression levels of ACSL4 in HT22 cells or cortical neurons were markedly elevated while SLC7A11 and GPX4 were inhibited by hemin, and PAN partially inhibited this phenomenon (Figure 4I). However, the inhibitory effect of PAN on the expression of these three proteins was reversed by ACSL4 overexpression (Figure 4I). In summary, overexpression of ACSL4 significantly reversed the PAN-induced inhibition of ferroptosis in hemin-treated neuronal cells.

HOTAIR Directly Bound to UPF1

To explore the location of HOTAIR, FISH and qRT-PCR were used. The data showed that HOTAIR was extensively distributed in the cytoplasm of HT22 cells (Figure 5A and B). Moreover, RIP and RNA pull-down assays demonstrated that HOTAIR directly bound to UPF1 (Figure 5C and D). In addition, HOTAIR was co-localized with UPF1 in HT22 cells (Figure 5E). In summary, HOTAIR directly bound to UPF1.

UPF1 Directly Bound and Destabilized ACSL4 mRNA

As indicated in Figure 6A and C, the expression of UPF1 in neuronal cells was reduced by UPF1 knockdown but upregulated by UPF1 overexpression. In addition, UPF1

knockdown significantly increased the expression of ACSL4, while UPF1 overexpression exhibited the opposite effect (Figure 6B and C). Meanwhile, UPF1 directly bound to ACSL4 (Figure 6D). Furthermore, overexpression of UPF1 significantly promoted the degradation of ACSL4 (Figure 6E). Taken together, these results suggest that UPF1 promoted the degradation of ACCSL4 mRNA by directly binding to ACSL4.

Overexpression of HOTAIR Significantly Reversed the Inhibitory Effect of PAN on Neuronal Cell Ferroptosis via the UPF1/ACSL4 Axis

To detect the expression of UPF1 and ACSL4, qRT-PCR was performed. As indicated in Figure 7A, after hemin and PAN co-treatment, the expression of UPF1 mRNA in neuronal cells was obviously decreased by the overexpression of HOTAIR, while the effect of HOTAIR overexpression was reversed by UPF1 overexpression. In contrast, HOTAIR overexpression notably increased the expression of ACSL4 mRNA, while this phenomenon was reversed by UPF1 overexpression. Moreover, the viability of neuronal cells was significantly inhibited by HOTAIR overexpression following treatment with PAN and hemin, and this effect was reversed when cells were transfected with the UPF1 overexpression vector (Figure 7B). In contrast, the HOTAIR-induced increase
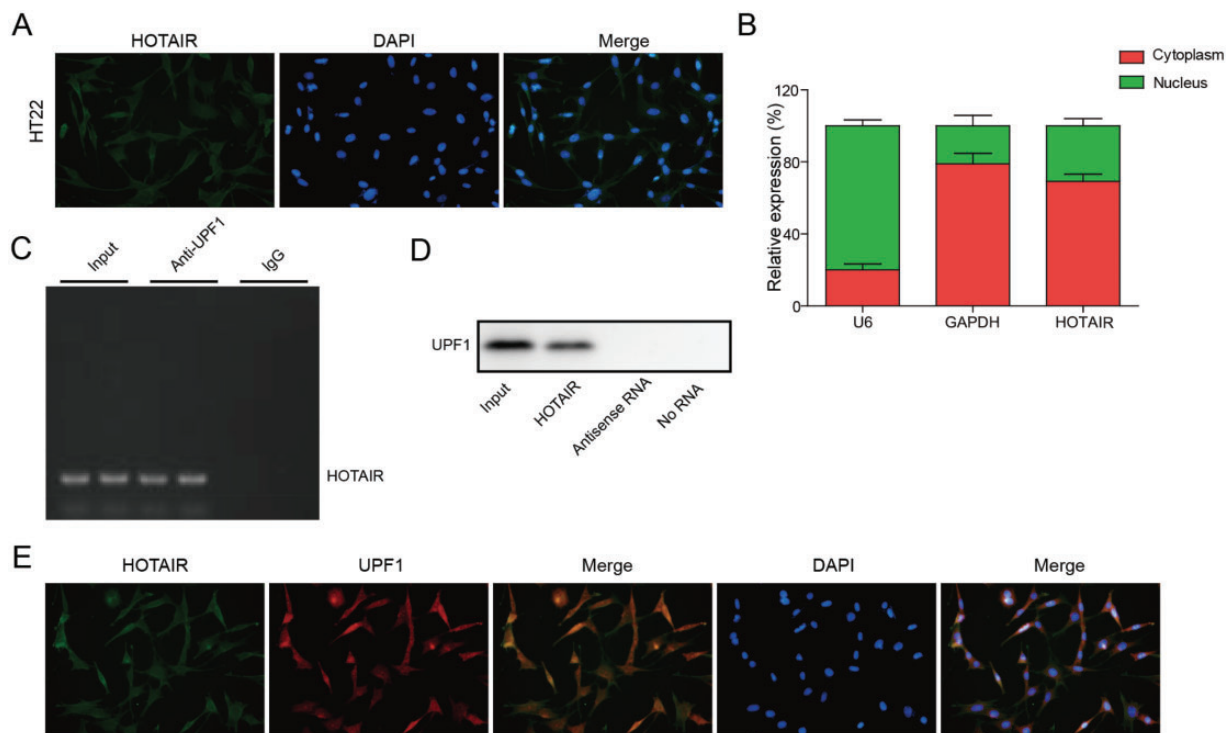

Figure 5. HOTAIR Directly Bound to UPF1. (A, B) The location of HOTAIR in HT22 cells was explored by FISH and qRT-PCR. (C, D) The correlation between HOTAIR and UPF1 in HT22 cells was explored by RNA pull-down and RIP assays. (E) The co-localization between HOTAIR and UPF1 was confirmed by immunofluorescence staining. (n = 3 in every group).
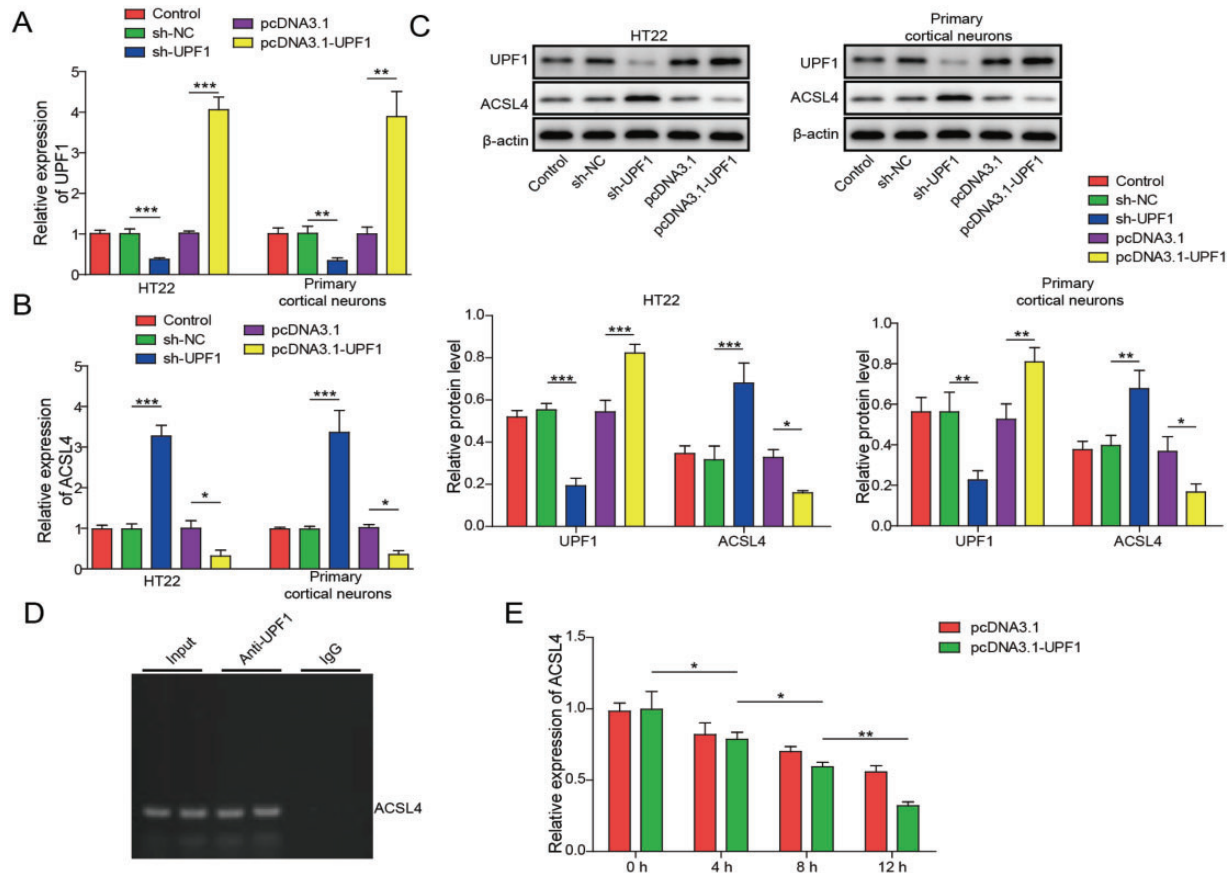
Figure 6. UPF1 Directly Bound to ACSL4. (A) HT22 cells or cortical neurons were transfected with sh-UPF1 or pcDNA3.1-UPF1. Then, UPF1 mRNA level was detected by qRT-PCR. (B) The mRNA level of ACSL4 in neuronal cells was assessed by qRT-PCR. (C) UPF1 and ACSL4 expression was assessed by western blot. β-actin was used for normalization. (D) RIP assay was used to explore the correlation between UPF1 and ACSL4. (E) ACSL4 mRNA levels in HT22 cells were measured by qRT-PCR at 4, 8 or 12 h after actinomycin D treatment. $^*P<0.05$, $^{**}P<0.01$, $^{***}P<0.001$. (n = 3 in every group). One-way analysis of variance (ANOVA) and Student's *t*-test were performed to analyse the data.

in MDA and ROS levels in neurons in the presence of PAN and hemin was inhibited by UPF1 upregulation (Figure 7C and D). Additionally, the injury (i.e., GSH depletion and iron accumulation) of neuronal cells following treatment with PAN and hemin was exacerbated by HOTAIR overexpression, while the effect of HOTAIR was partially inhibited by UPF1 overexpression (Figure 7E and F). Furthermore, the protein expression levels of ACSL4 in neuronal cells following hemin and PAN treatment were significantly upregulated while SLC7A11 and GPX4 were downregulated by HOTAIR overexpression, while this phenomenon was rescued by pcDNA3.1-UPF1 (Figure 7G). In contrast, overexpression of HOTAIR notably decreased UPF1 protein levels in neurons following treatment with hemin and PAN, while the effect of HOTAIR overexpression was inhibited by UPF1 overexpression (Figure 7G). In summary, overexpression of HOTAIR significantly reversed the

inhibitory effect of PAN on neuronal cell ferroptosis via the UPF1/ACSL4 axis.

Discussion

In the current study, we found that PAN inhibited ICH progression. In addition, PAN inhibited ferroptosis in neurons, while HOTAIR overexpression reversed this phenomenon. Meanwhile, UPF1 and ACSL4 were found to be downstream targets of HOTAIR in ICH. Our findings provide a new idea for the treatment of ICH.

Ferroptosis is known as a type of cell death (Verma et al., 2020). In addition, it has been previously confirmed that ferroptosis is involved in the progression of ICH (Z. Li et al., 2020; Mohammed Thangameeran et al., 2020), and this background indicates that ferroptosis is a key process in ICH-induced neuronal injury. A previous report showed that PAN inhibited the progression of
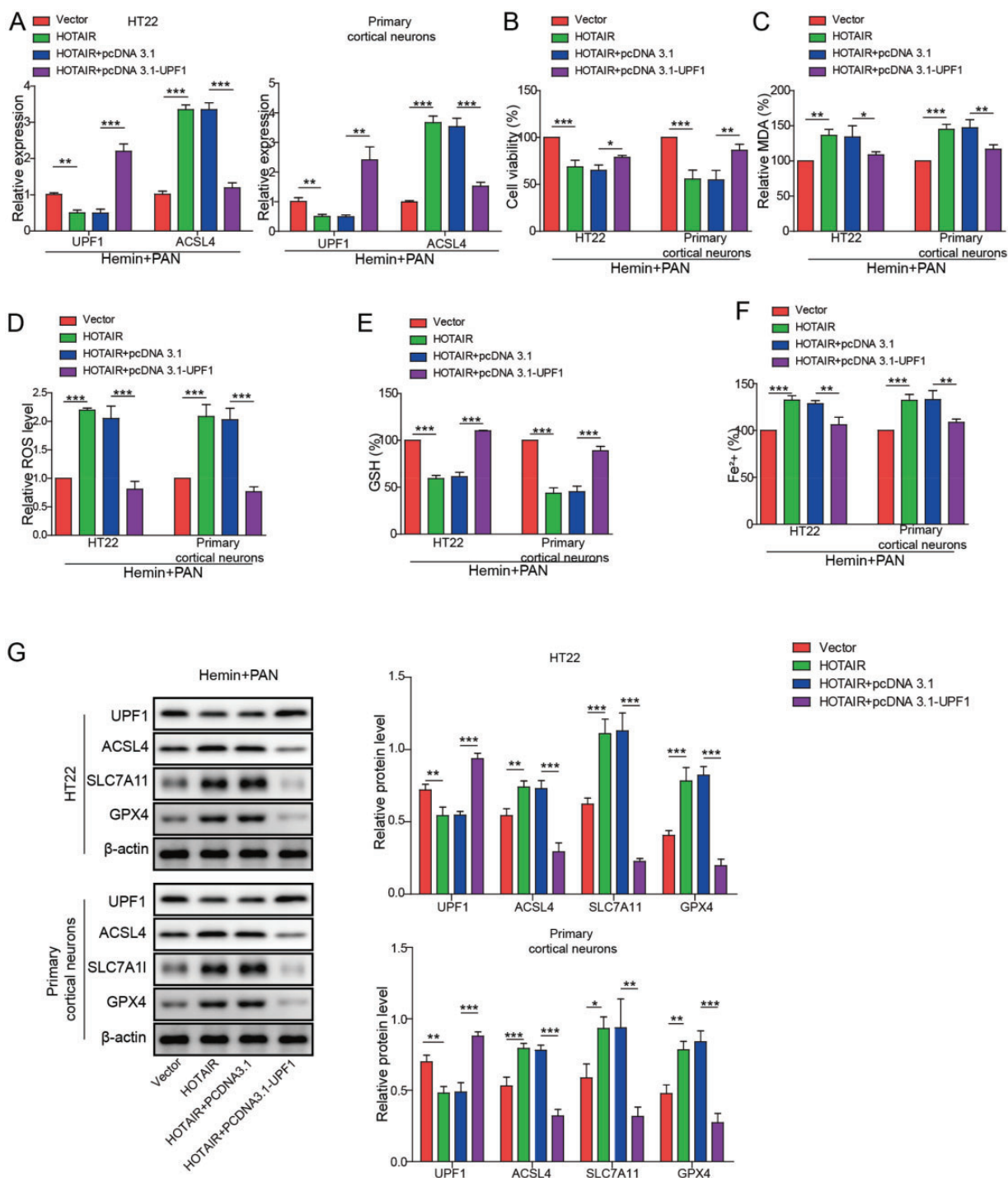
Figure 7. Overexpression of HOTAIR Significantly Reversed the Inhibitory Effect of PAN on Neuronal Ferroptosis by Mediating the UPF1/ACSL4 Axis. (A) The expression of UPF1 and ACSL4 in neuronal cells following treatment with hemin and PAN was assessed by qRT-PCR. (B) Neuronal cell viability was tested by MTT assay. (C) The MDA level was tested by a Lipid Peroxidation Assay Kit. (D) The lipid ROS level was detected by flow cytometry. (E) The GSH level in neuronal cells was measured by Glutathione Assay Kit. (F) The Fe^{2+} content of neuronal cells was assessed by an Iron Assay Kit. (G) UPF1, ACSL4, SLC7A11 and GPX4 expression in neuronal cells was measured by western blot. β-actin was used for normalization. $^{*}P<0.05$, $^{**}P<0.01$, $^{***}P<0.001$. (n = 3 in every group). One-way analysis of variance (ANOVA) and Student's t-test were performed to analyse the data.

inflammation and cancer (M. Cai et al., 2020; Shi et al., 2020; J. J. Zhang et al., 2020). Moreover, Li X et al found that PAN inhibited cell injury during ICH progression (Li et al., 2018). Our research is the first to find that PAN alleviates ferroptosis in ICH, which supplements our knowledge of the underlying mechanism of PAN in ICH. It has been reported that HOTAIR participates in inflammation and cancers (L. Cai et al., 2020; Takei et al., 2020). In addition, it has been reported that HOTAIR is involved in ischaemic infarct (Yang and Lu, 2016). In this study, HOTAIR overexpression was found to reverse the effect of PAN on ICH by inducing ferroptosis. Therefore, our study is the first to suggest a correlation between HOTAIR and ferroptosis in ICH, which indicates that HOTAIR could act as a promoter in ICH.

Moreover, UPF1 is known to be involved in the NMD pathway (Fefilova et al., 2020; Zou et al., 2020). In addition, UPF1 has been confirmed to act as an inhibitor in malignant tumours (Z. Sun et al., 2020; Zhong et al., 2020). A previous study indicated that lncRNA ZFPM2-AS1 promoted lung adenocarcinoma progression by interacting with UPF1 to regulate the mRNA decay of ZFPM2 (Han et al., 2020). Similarly, our research found that HOTAIR bound to UPF1. Moreover, our data revealed that UPF1 promoted the degradation of ACSL4. Taken together with the above results, these findings suggest that HOTAIR might positively regulate ACSL4 by competitively binding to UPF1, whereas ACSL4 has been confirmed to be a promoter of cell ferroptosis (X. Chen et al., 2020; Tang et al., 2020). Finally, *in vitro* rescue assays confirmed that HOTAIR positively regulated neuronal ferroptosis through the UPF1/ACSL4 axis.

There are some limitations in this research. For instance, the miRNAs sponged by HOTAIR in ICH need to be found. In addition, more signalling pathways mediated by HOTAIR in ICH remain to be explored. Therefore, more investigations are needed in the future.

In conclusion, PAN inhibits the progression of ICH via the HOTAIR/UPF1/ACSL4 signalling pathway. Thus, PAN could act as a new agent for the treatment of ferroptosis in ICH.

Summary Statement

In the current study, we found paeonol (PAN) inhibited ICH progression in HT22 cells. PAN inhibited ferroptosis, while HOTAIR overexpression reversed this phenomenon in HT22 cells. Additionally, UPF1 and ACSL4 were found to be downstream targets of HOTAIR in ICH.

Author Contributions

Conception and study design: Zheng-Long Jin, Wen-Ying Gao; data acquisition: Shao-Jun Liao; data analysis: Tao Yu, Qing Shi; manuscript drafting: Shang-Zhen Yu; manuscript revising: Ye-Feng Cai.

Data Accessibility Statement

Ethical Approval

Declaration of Conflicting Interests

Funding

ORCID iD

Ye-Feng Cai 🆔 https://orcid.org/0000-0003-3658-2738

References

Alzahrani, F., Kuwahara, H., Long, Y., Al-Owain, M., Tohary, M., AlSayed, M., Mahnashi, M., Fathi, L., Alnemer, M., Al-Hamed, M. H., Lemire, G., Boycott, K. M., Hashem, M., Han, W., Al-Maawali, A., Al Mahrizi, F., Al-Thihli, K., Gao, X., & Alkuraya, F. S. (2020). Recessive, deleterious variants in SMG8 expand the role of nonsense-mediated decay in developmental disorders in humans. *Am J Hum Genet*, 107, 1178–1185.

Cai, L., Tu, L., Yang, X., Zhang, Q., Tian, T., Gu, R., Qu, X., Wang, Q., & Tian, J. (2020). HOTAIR accelerates dyskinesia in a mptp-lesioned mouse model of PD via SSTR1 methylation-mediated ERK1/2 axis. *Mol Ther Nucleic Acids*, 22, 140–152.

Cai, M., Shao, W., Yu, H., Hong, Y., & Shi, L. (2020). paeonol inhibits cell proliferation, migration and invasion and induces apoptosis in hepatocellular carcinoma by regulating miR-21-5p/KLF6 axis. *Cancer Manag Res*, 12, 5931–5943.

Cassetta, L., et al. (2020). Differential expansion of circulating human MDSC subsets in patients with cancer, infection and inflammation. *J Immunother Cancer*, 8. https://doi.org/10.1136/jitc-2020-001223

Chen, J. X., Wang, Y. P., Zhang, X., Li, G. X., Zheng, K., & Duan, C. Z. (2020). lncRNA Mtss1 promotes inflammatory responses and secondary brain injury after intracerebral hemorrhage by targeting miR-709 in mice. *Brain Res Bull*, 162, 20–29.

Chen, X., Li, J., Kang, R., Klionsky, D. J., & Tang, D. (2020). Ferroptosis: Machinery and regulation. *Autophagy*, 16, 1–28.

Cheng, J., Fan, Y. Q., Liu, B. H., Zhou, H., Wang, J. M., & Chen, Q. X. (2020). ACSL4 suppresses glioma cells proliferation via activating ferroptosis. *Oncol Rep*, *43*, 147–158.

Chu, C. L., Chen, Y. P., Chen, C. C. P., Chen, C. K., Chang, H. N., Chang, C. H., & Pei, Y. C. (2020). Functional recovery patterns of hemorrhagic and ischemic stroke patients under post-acute care rehabilitation program. *Neuropsychiatr Dis Treat*, *16*, 1975–1985.

Cordeiro, J. L., Neves, J. D., Nicola, F., Vizuete, A. F., Sanches, E. F., Goncalves, C. A., & Netto, C. A. (2020). Arundic acid (ONO-2506) attenuates neuroinflammation and prevents motor impairment in rats with intracerebral hemorrhage. *Cell Mol Neurobiol*. https://doi.org/10.1007/s10571-020-00964-6

Cui, H., Yang, A., Zhou, H., Wang, Y., Luo, J., Zhou, J., Liu, T., Li, P., Zhou, J., Hu, E., He, Z., Hu, W., & Tang, T. (2020). Thrombin-induced miRNA-24-1-5p upregulation promotes angiogenesis by targeting prolyl hydroxylase domain 1 in intracerebral hemorrhagic rats. *J Neurosurg*, 1–12. https://doi.org/10.3171/2020.2.JNS193069

Deka, B., Chandra, P., & Singh, K. K. (2020). Functional roles of human up-frameshift suppressor 3 (UPF3) proteins: From nonsense-mediated mRNA decay to neurodevelopmental disorders. *Biochimie*, *180*, 10–22.

Fang, Y., Gao, S., Wang, X., Cao, Y., Lu, J., Chen, S., Lenahan, C., Zhang, J. H., Shao, A., & Zhang, J. (2020). programmed cell deaths and potential crosstalk with blood-brain barrier dysfunction after hemorrhagic stroke. *Front Cell Neurosci*, *14*, 68.

Fefilova, A., Melnikov, P., Prikazchikova, T., Abakumova, T., Kurochkin, I., Mazin, P. V., Ziganshin, R., Sergeeva, O., & Zatsepin, T. S. (2020). Murine long noncoding RNA morrbid contributes in the regulation of NRAS splicing in hepatocytes in vitro. *Int J Mol Sci*, *21*. https://doi.org/10.3390/ijms21165605

Han, S., Cao, D., Sha, J., Zhu, X., & Chen, D. (2020). LncRNA ZFPM2-AS1 promotes lung adenocarcinoma progression by interacting with UPF1 to destabilize ZFPM2. *Mol Oncol*, *14*, 1074–1088.

Hu, L., Zhang, H., Wang, B., Ao, Q., & He, Z. (2020). MicroRNA-152 attenuates neuroinflammation in intracerebral hemorrhage by inhibiting thioredoxin interacting protein (TXNIP)-mediated NLRP3 inflammasome activation. *Int Immunopharmacol*, *80*, 106141.

Kurt, S., Tomatir, A. G., Tokgun, P. E., & Oncel, C. (2020). Altered expression of long non-coding RNAs in peripheral blood mononuclear cells of patients with Alzheimer's disease. *Mol Neurobiol*. *57*, 5352–5361.

Lei, G., Zhang, Y., Koppula, P., Liu, X., Zhang, J., Lin, S. H., Ajani, J. A., Xiao, Q., Liao, Z., Wang, H., & Gan, B. (2020). The role of ferroptosis in ionizing radiation-induced cell death and tumor suppression. *Cell Res*, *30*, 146–162.

Li, M., Liu, G., Wang, K., Wang, L., Fu, X., Lim, L. Y., Chen, W., & Mo, J. (2020). Metal ion-responsive nanocarrier derived from phosphonated calix[4]arenes for delivering dauricine specifically to sites of brain injury in a mouse model of intracerebral hemorrhage. *J Nanobiotechnology*, *18*, 61.

Li, X., Huang, X., Tang, Y., Zhao, F., Cao, Y., Yin, L., & Li, G. (2018). Assessing the pharmacological and therapeutic efficacy of traditional Chinese medicine Liangxue Tongyu prescription for intracerebral hemorrhagic stroke in neurological disease models. *Front Pharmacol*, *9*, 1169.

Li, Z., Wu, G., Li, J., Wang, Y., Ju, X., & Jiang, W. (2020). lncRNA CRNDE promotes the proliferation and metastasis by acting as sponge miR-539-5p to regulate POU2F1 expression in HCC. *BMC Cancer*, *20*, 282.

Liu, M. M., Dong, R., Hua, Z., Lv, N. N., Ma, Y., Huang, G. C., Cheng, J., & Xu, H. Y. (2020). Therapeutic potential of Liuwei Dihuang Pill against KDM7a and Wnt/beta-catenin signaling pathway in diabetic nephropathy-related osteoporosis. *Biosci Rep*, *40*. https://doi.org/10.1042/BSR20201778

Lorente, L., Martin, M. M., Perez-Cejas, A., Gonzalez-Rivero, A. F., Sabatel, R., Ramos-Gomez, L., Argueso, M., Sole-Violan, J., Caceres, J. J., Jimenez, A., & Garcia-Marin, V. (2020). High serum levels of TAC and early mortality in patients with spontaneous intracerebral haemorrhage. *Neurol Sci*. *34*, 175–181.

Mi, J., Han, Y., Zhang, J., Hao, X., Xing, M., & Shang, C. (2020). Long noncoding RNA LINC01410 promotes the tumorigenesis of neuroblastoma cells by sponging microRNA-506-3p and modulating WEE1. *Cancer Med*. *9*, 8133–8143.

Mohammed Thangameeran, S. I., Tsai, S. T., Hung, H. Y., Hu, W. F., Pang, C. Y., Chen, S. Y., & Liew, H. K. (2020). A role for endoplasmic reticulum stress in intracerebral hemorrhage. *Cells*, *9*. https://doi.org/10.3390/cells9030750

Morsy, M. A., Abdel-Aziz, A. M., Abdel-Hafez, S. M. N., Venugopala, K. N., Nair, A. B., & Abdel-Gaber, S. A. (2020). The possible contribution of P-glycoprotein in the protective effect of paeonol against methotrexate-induced testicular injury in rats. *Pharmaceuticals (Basel)*, *13*. https://doi.org/10.3390/ph13090223

Pasi, M., Casolla, B., Kyheng, M., Boulouis, G., Kuchcinski, G., Moulin, S., Labreuche, J., Henon, H., Cordonnier, C., & Leys, D. (2020). Long-term mortality in survivors of spontaneous intracerebral hemorrhage. *Int J Stroke*, 1747493020954946.

Shi, X., Xie, X., Sun, Y., He, H., Huang, H., Liu, Y., Wu, H., & Dai, M. (2020). Paeonol inhibits NLRP3 mediated inflammation in rat endothelial cells by elevating hyperlipidemic rats plasma exosomal miRNA-223. *Eur J Pharmacol*, *885*, 173473.

Su, X., Wang, H., Lin, Y., & Chen, F. (2018). RIP1 and RIP3 mediate hemin-induced cell death in HT22 hippocampal neuronal cells. *Neuropsychiatr Dis Treat*, *14*, 3111–3119.

Sun, X., Gan, L., Li, N., Sun, S., & Li, N. (2020). Tabersonine ameliorates osteoblast apoptosis in rats with dexamethasone-induced osteoporosis by regulating the Nrf2/ROS/Bax signalling pathway. *AMB Express*, *10*, 165.

Sun, Z., Wu, K., Gu, L., Huang, L., Zhuge, Q., Yang, S., & Wang, Z. (2020). IGF-1R stimulation alters microglial polarization via TLR4/NF-kappaB pathway after cerebral hemorrhage in mice. *Brain Res Bull*, *164*, 221–234.

Sykora, M., Szabo, J., Siarnik, P., Turcani, P., Krebs, S., Lang, W., Czosnyka, M., & Smielewski, P. (2020). Heart rate

entropy is associated with mortality after intracereberal hemorrhage. *J Neurol Sci*, *418*, 117033.

Takei, Y., Hara, T., Suzuki, A., Mihara, K., & Yanagihara, K. (2020). Long noncoding RNA HOTAIR promotes epithelial-mesenchymal transition and is a suitable target to inhibit peritoneal dissemination in human scirrhous gastric cancers. *Pathobiology*, *87*, 1–14.

Tang, L. J., Luo, X. J., Tu, H., Chen, H., Xiong, X. M., Li, N. S., & Peng, J. (2020). Ferroptosis occurs in phase of reperfusion but not ischemia in rat heart following ischemia or ischemia/reperfusion. *Naunyn Schmiedebergs Arch Pharmacol*. https://doi.org/10.1007/s00210-020-01932-z

Verma, N., Vinik, Y., Saroha, A., Nair, N. U., Ruppin, E., Mills, G., Karn, T., Dubey, V., Khera, L., Raj, H., Maina, F., & Lev, S. (2020). Synthetic lethal combination targeting BET uncovered intrinsic susceptibility of TNBC to ferroptosis. *Sci Adv*, *6*.

Wang, X., Yu, X., Wei, W., & Liu, Y. (2020). Long noncoding RNA MACC1-AS1 promotes the stemness of nonsmall cell lung cancer cells through promoting UPF1-mediated destabilization of LATS1/2. *Environ Toxicol*, *35*, 998–1006.

Wang, Y., Wang, Y., Luo, W., Song, X., Huang, L., Xiao, J., Jin, F., Ren, Z., & Wang, Y. (2020). Roles of long noncoding RNAs and emerging RNA-binding proteins in innate antiviral responses. *Theranostics*, *10*, 9407–9424.

Xiang, W., Lyu, L., Huang, T., Zheng, F., Yuan, J., Zhang, C., & Jiang, G. (2020). The long non-coding RNA SNHG1 promotes bladder cancer progression by interacting with miR-143-3p and EZH2. *J Cell Mol Med*, *24*, 11858–11873.

Yang, L., & Lu, Z. N. (2016). Long non-coding RNA HOTAIR promotes ischemic infarct induced by hypoxia through up-regulating the expression of NOX2. *Biochem Biophys Res Commun*, *479*, 186–191.

Yoshimoto, T., Tanaka, K., Yamagami, H., Uchida, K., Inoue, M., Koge, J., Ihara, M., Toyoda, K., Imamura, H., Ohara, N., Morimoto, T., Sakai, N., & Yoshimura, S. (2020). Treatment outcomes by initial neurological deficits in acute stroke patients with basilar artery occlusion: The RESCUE Japan Registry 2. *J Stroke Cerebrovasc Dis*, *29*, 105256.

Yu, Y., Yan, R., Chen, X., Sun, T., & Yan, J. (2020). Paeonol suppresses the effect of ox-LDL on mice vascular endothelial cells by regulating miR-338-3p/TET2 axis in atherosclerosis. *Mol Cell Biochem*, *475*, 127–135.

Yuan, H., Li, X., Zhang, X., Kang, R., & Tang, D. (2016). Identification of ACSL4 as a biomarker and contributor of ferroptosis. *Biochem Biophys Res Commun*, *478*, 1338–1343.

Zhang, J., Dong, B., Hao, J., Yi, S., Cai, W., & Luo, Z. (2019). LncRNA Snhg3 contributes to dysfunction of cerebral microvascular cells in intracerebral hemorrhage rats by activating the TWEAK/Fn14/STAT3 pathway. *Life Sci*, *237*, 116929.

Zhang, J., Shan, H., Tao, L., & Zhang, M. (2020). Biological effects of hydrogen sulfide and its protective role in intracerebral hemorrhage. *J Mol Neurosci*. *70*, 2020–2030.

Zhang, J. J., Cai, L. J., Pang, K., Dong, Y., Zhang, Z. G., Li, B. B., Li, R., & Han, C. H. (2020). Paeonol inhibits proliferation and induces cell apoptosis of human T24 and 5637 bladder cancer cells in vitro and in vivo. *Clin Transl Oncol*. *23*, 601–611.

Zhao, X., Kruzel, M. L., & Aronowski, J. (2020). Lactoferrin and hematoma detoxification after intracerebral hemorrhage. *Biochem Cell Biol*. *99*, 97–101.

Zhong, Z. B., Wu, Y. J., Luo, J. N., Hu, X. N., Yuan, Z. N., Li, G., Wang, Y. W., Yao, G. D., & Ge, X. F. (2020). Knockdown of long noncoding RNA DLX6-AS1 inhibits migration and invasion of thyroid cancer cells by upregulating UPF1. *Eur Rev Med Pharmacol Sci*, *24*, 8246.

Zhou, H., Qiu, Z. Z., Yu, Z. H., Gao, L., He, J. M., Zhang, Z. W., & Zheng, J. (2019). Paeonol reverses promoting effect of the HOTAIR/miR-124/Notch1 axis on renal interstitial fibrosis in a rat model. *J Cell Physiol*, *234*, 14351–14363.

Zou, Y., Ruan, S., Jin, L., Chen, Z., Han, H., Zhang, Y., Jian, Z., Lin, Y., Shi, N., & Jin, H. (2020). CDK1, CCNB1, and CCNB2 are prognostic biomarkers and correlated with immune infiltration in hepatocellular carcinoma. *Med Sci Monit*, *26*, e925289.